Letter

Chern mosaic and ideal flat bands in equal-twist trilayer graphene

Daniele Guerci [1], Yuncheng Mao [2], and Christophe Mora [2]

[1] *Center for Computational Quantum Physics, Flatiron Institute, New York, New York 10010, USA*

[2] *Université Paris Cité, CNRS, Laboratoire Matériaux et Phénomènes Quantiques, 75013 Paris, France*

(Received 12 May 2023; accepted 25 January 2024; published 30 April 2024)

We study trilayer graphene arranged in a staircase stacking configuration with equal consecutive twist angle. On top of the moiré crystalline pattern, a supermoiré long-wavelength modulation emerges that we treat adiabatically. For each valley, we find that the two central bands are topological with Chern numbers $C = \pm 1$ forming a Chern mosaic at the supermoiré scale. The Chern domains are centered around the high-symmetry stacking points ABA or BAB and they are separated by gapless lines connecting the AAA points where the spectrum is fully connected. In the chiral limit and at a magic angle of $\theta \sim 1.69^\circ$, we prove that the central bands are exactly flat with ideal quantum curvature at ABA and BAB. Furthermore, we decompose them analytically as a superposition of an intrinsic color-entangled state with ± 2 and a Landau level state with Chern number ∓ 1. To connect with experimental configurations, we also explore the nonchiral limit with finite corrugation and find that the topological Chern mosaic pattern is indeed robust and the central bands are still well separated from the remote bands.

DOI: 10.1103/PhysRevResearch.6.L022025

Introduction. Stacking and twisting two layers of graphene realizes an extraordinary platform [1] which, in the magic angle region, gives rise to flat bands [2–7] hosting superconductivity [8–12], interaction-driven insulating states [13–22], anomalous Hall effects [23–32], and fractional Chern insulators [33–35]. The intimate connection between the flat bands of twisted bilayer graphene (TBG) and the properties of Landau levels [36–51] played a key role for the understanding of the interplay between correlation and topology in the aforementioned correlated states. Following this guiding principle, we characterized the properties of the flat bands in equal-twist staircase trilayer graphene (eTTG) sketched in Fig. 1(a), finding high-symmetry stacking ABA/BAB configurations with total Chern number ± 1 hosting an intrinsic color-entangled state [52–55] with Chern number 2 and a Landau level like state with Chern number -1.

Adding an additional graphene sheet to TBG rotated by a small relative twist angle [twisted trilayer graphene (TTG)] gives rise to the superposition of two moiré superlattices [56,57]. With the exception of mirror-symmetric TTG [58–67] and twisted monobilayer graphene [68–71], the two moiré periodicities are incommensurate [72,73], leading to a quasicrystalline structure that dominates the electronic behavior at relevant energies [57]. The theoretical description of twisted trilayer graphene runs into fundamental difficulties [72,73] due to the quasiperiodic nature of the low-energy Hamiltonian, disallowing all the simplifications from Bloch's theorem. Similar effects can also emerge in TBG aligned with hBN [74,75].

The aim of this Letter is to study the emergent effect of the superposition of the two moiré patterns in eTTG. The system is the simplest example of a quasiperiodic moiré crystal [72] where the angle θ_{12}, between layer one (top) and two (middle), and θ_{23}, between layer two and three (bottom), are equal $\theta_{12} = \theta_{23} \equiv \theta$. In the magic angle region, where $\theta \approx 1^\circ$, the two incommensurate periodicity can be decomposed in a fast modulation $\boldsymbol{q}_j$ on the moiré scale $|\boldsymbol{q}_j| \propto \theta$ and a slow one $\delta\boldsymbol{q}_j$ with much larger periodicity $|\delta\boldsymbol{q}_j| \propto \theta^2$ [73,76]. Within a semiclassical adiabatic approximation [77–81], we define a local Hamiltonian $H_{\mathrm{eTTG}}(\boldsymbol{r}) = H_{\mathrm{eTTG}}(\boldsymbol{r}, \boldsymbol{\phi})$ where $\boldsymbol{\phi}$ depends on the slowly varying supermoiré scale [73]. In this picture, we obtain a Chern number versus $\boldsymbol{\phi}$ real-space map Fig. 1(b) that gives rise to a Chern mosaic of triangular regions with ± 1 Chern number. Figure 1(c) shows the energy gap between the flat bands and the remote ones which takes the maximum value for ABA and BAB sites. Furthermore, the domain walls separating the topological regions close the gap E_{gap} to the remote bands and form lines connecting the AAA centers. The ABA and BAB stacking configurations, exhibiting the largest energy gap E_{gap}, are expected to be favored by lattice relaxation [82,83]. Some of our findings can be generalized to cases involving unequal twist angles [73,84].

There are three high-symmetry stacking configurations that are especially significant and indicative of the Chern mosaic pattern: AAA, ABA, and BAB. We explore them analytically in the chiral limit to unveil the topological features of the mosaic. We thereby derive analytical expressions for the resulting ideal flat bands emerging at a magic angle. The AAA stacking, considered in the preprint [85], is characterized by a vanishing Berry curvature and a fully connected spectrum protected by $C_{2z}T$ [86]. At the magic angle $\theta_{\mathrm{AAA}} \approx 0.75^\circ$ a fourfold

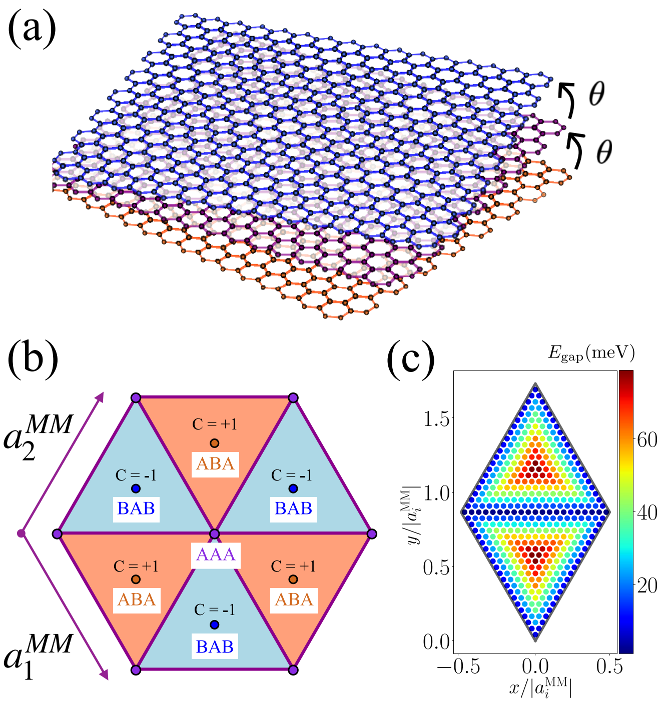

FIG. 1. (a) Equal-twist angle trilayer graphene lattice in real space. (b) Real-space Chern mosaic and (c) energy gap over the supermoiré lattice computed for $\theta = 1.69^\circ$ and $w_{\rm AA} = 0.6 w_{\rm AB}$. Regions around ABA (BAB) stackings host a pair of isolated nearly flat bands with total Chern number $+1$ (-1). Topological transitions occur at domain wall (magenta) lines where the gap $E_{\rm gap}$ closes and the spectrum is fully connected.

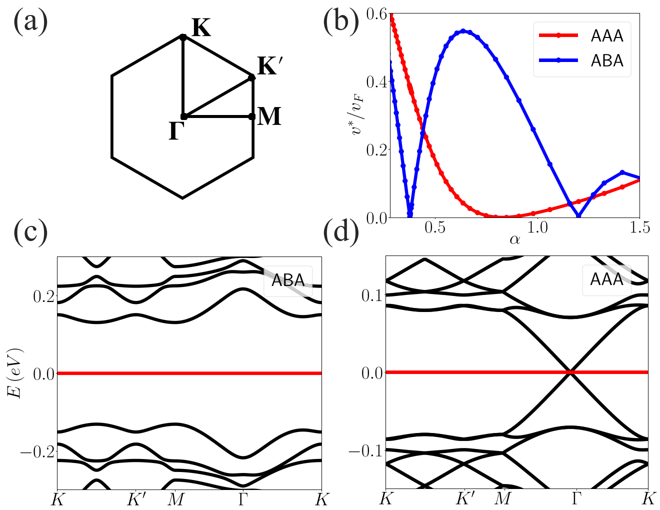

FIG. 2. (a) Mini moiré Brillouin zone (BZ). (b) Renormalized velocity v^* for AAA (red) and ABA (blue) regions as a function of the dimensionless coupling $\alpha = w_{AB}/v_F k_\theta$ and $w_{AA} = 0$ (chiral limit). Dispersion relation for ABA stacking (c) and AAA stacking (d) at the magic angle $\theta_{\rm AAA} \approx 0.75^\circ$ and $\theta_{\rm ABA} \approx 1.69^\circ$, respectively.

degenerate zero energy flat band sector emerges, connected to a single Dirac cone. The ABA (BAB) stacking, on the other hand, shows a flat band region detached from the remote bands with total Chern number $C = 1(-1)$. The origin of the finite Chern number is readily traced out by the nature of the flat bands at the magic angle $\theta_{\rm ABA} \approx 1.69^\circ$ which, remarkably, is larger than the one in mirror-symmetric TTG [43]. We prove that the flat band sector decomposes into a Chern $+2(-2)$ color-entangled zero mode [55,87,88] and a Chern $-1(+1)$ Landau level like state [36,38,39,48,49,51,89,90]. The resulting imbalance in Chern flux creates a Chern mosaic pattern in real space, which could be detected by measuring the local orbital magnetization in real space [27,28].

Chern Mosaic on the supermoiré scale. When the twist angle is small, noncommensurability effects are characterized by a length scale well separated from the moiré scale, $|\delta \boldsymbol{q}_j|/|\boldsymbol{q}_j| \approx 0.02$ for $\theta = 1^\circ$. As a result, the long wavelength modulation can be treated parametrically, leading to the local Hamiltonian for a single valley obtained in Ref. [73]:

$$H_{\rm eTTG}(\boldsymbol{r}, \boldsymbol{\phi}) = \begin{pmatrix} v_F \hat{\boldsymbol{k}} \cdot \boldsymbol{\sigma} & T(\boldsymbol{r}, \boldsymbol{\phi}) & 0 \\ h.c. & v_F \hat{\boldsymbol{k}} \cdot \boldsymbol{\sigma} & T(\boldsymbol{r}, -\boldsymbol{\phi}) \\ 0 & h.c. & v_F \hat{\boldsymbol{k}} \cdot \boldsymbol{\sigma} \end{pmatrix}, \tag{1}$$

where the other valley is obtained by time-reversal symmetry. $v_F \approx 10^6\,{\rm m/s}$ is the graphene velocity and the phases $\boldsymbol{\phi} = (\phi_1, \phi_2, \phi_3)$ defines the local stacking configuration [73,76]. Varying $\boldsymbol{\phi}$ maps out the supermoiré unit cell in Fig. 1(b), $\boldsymbol{\sigma}$ is the vector of Pauli matrices in the sublattice space, and $\hat{\boldsymbol{k}} = -i\nabla_{\boldsymbol{r}}$. The tunneling between different layers is described by the moiré potential

$$T(\boldsymbol{r}, \boldsymbol{\phi}) = \sum_{j=1}^{3} T_j e^{-i\boldsymbol{r}\cdot\boldsymbol{q}_j} e^{-i\phi_j}, \tag{2}$$

where $T_{j+1} = w_{\rm AA}\sigma^0 + w_{\rm AB}[\sigma^x \cos 2\pi j/3 + \sigma^y \sin 2\pi j/3]$, $w_{\rm AB} = 110\,{\rm meV}$, using complex notation $\boldsymbol{q}_{j+1} = i\omega^j$ [86] with $\omega = e^{2i\pi/3}$ and $j = 0, 1, 2$, in units of $k_\theta = \theta K_D$ with a K_D Dirac cone of graphene. The moiré lattice is characterized by the reciprocal lattice vectors $\boldsymbol{b}_{1/2} = \boldsymbol{q}_1 - \boldsymbol{q}_{2/3}$ and primitive vectors $\boldsymbol{a}_{1/2}$. The wavefunctions satisfy Bloch periodicity and particle-hole symmetry denoted P [76]. At low-energy the model (1) is characterized by three inequivalent Dirac cones at K, K', and Γ of the mini Brillouin zone (BZ) shown in Fig. 2(a). The central one at Γ is protected by P while K and K' are gapped for generic $\boldsymbol{\phi}$ [73].

We now obtain the spectrum of the Hamiltonian (1) and study the topological properties of the nearly flat bands around charge neutrality. Figure 1(b) shows the real-space mosaic pattern obtained by computing the Chern number $\mathcal{C}(\boldsymbol{\phi})$ for the two central bands at the magic angle $\theta_{\rm ABA} = 1.69^\circ$ for finite corrugation $w_{\rm AA} = 0.6 w_{\rm AB}$. The mosaic exhibits a triangular periodic structure, which is generated by the lattice vectors $\mathbf{a}^{\rm MM}_{1/2} = 4\pi e^{\mp i\pi/3}/3k^{\rm MM}_\theta$, where $k^{\rm MM}_\theta = \theta^2 K_D$. The two central bands are topological everywhere except along lines connecting the AAA centers, where the gap with the remote bands closes as shown in Fig. 1(c) and the spectrum is fully connected. Each topological region is centered around $\mathbf{r}_{\rm ABA} = (\mathbf{a}^{\rm MM}_2 - \mathbf{a}^{\rm MM}_1)/3$ and $\mathbf{r}_{\rm BAB} = -\mathbf{r}_{\rm ABA}$, with opposite Chern numbers of ± 1. To uncover the nature of the topological bands, we specifically focus on these two high-symmetry stackings. Moreover, we consider the chiral limit, where the bands become exactly flat and an analytical solution can be obtained.

ABA stacking: color-entangled flat band. The ABA region is described by the local Hamiltonian $\mathcal{H}_{\mathrm{ABA}}$ obtained from Eq. (1) with $\boldsymbol{\phi} = 2\pi/3(0, 1, -1)$. Here, the C_{3z} symmetry is recovered while C_{2x} and $C_{2z}T$ are broken. The latter connects ABA to BAB explaining the opposite Chern numbers of the ABA and BAB regions. The combination of C_{2x} and $C_{2z}T$ is a symmetry for the model $C_{2y}T$ which, together with P and C_{3z}, protects three Dirac cones at Γ, K, and K' [76]. We henceforth consider the chiral limit $w_{\mathrm{AA}} = 0$ where an inspiring mathematical structure emerges [36]. $\mathcal{H}_{\mathrm{ABA}}$ then anticommutes with the chiral operator $\Lambda^z = \mathbf{1} \otimes \sigma^z$ with $\mathbf{1}$ the identity in the layer basis. Denoting with ψ_l and χ_l with $l = 1, 2, 3$ the wavefunction components polarized in the A and B sublattices, in the basis $\Psi = (\psi_1 \quad \psi_2 \quad \psi_3 \quad \chi_1 \quad \chi_2 \quad \chi_3)^T$ the Hamiltonian $\mathcal{H}_{\mathrm{ABA}}$ reads

$$\frac{\mathcal{H}_{\mathrm{ABA}}(\boldsymbol{r})}{v_F k_\theta} = \begin{pmatrix} 0 & \mathcal{D}_1(\boldsymbol{r}) \\ \mathcal{D}_1^\dagger(\boldsymbol{r}) & 0 \end{pmatrix}, \tag{3}$$

and we look for zero-mode solutions,

$$\mathcal{D}_1(\boldsymbol{r})\boldsymbol{\chi}_{\boldsymbol{k}}(\boldsymbol{r}) = 0, \quad \mathcal{D}_1^\dagger(\boldsymbol{r})\boldsymbol{\psi}_{\boldsymbol{k}}(\boldsymbol{r}) = 0, \tag{4}$$

constrained to the Bloch-periodic boundary conditions detailed in the SM [76]. In Eq. (3) we have introduced

$$\mathcal{D}_1(\boldsymbol{r}) = \begin{pmatrix} -i\sqrt{2}\partial & U_\omega(\boldsymbol{r}) & 0 \\ U_0(-\boldsymbol{r}) & -i\sqrt{2}\partial & U_0(\boldsymbol{r}) \\ 0 & U_\omega(-\boldsymbol{r}) & -i\sqrt{2}\partial \end{pmatrix}, \tag{5}$$

with $\partial = (\partial_x - i\partial_y)/(\sqrt{2}k_\theta)$, $z = k_\theta(x+iy)/\sqrt{2}$, $U_0(\boldsymbol{r}) = \alpha\sum_{j=1}^3 e^{-i\boldsymbol{q}_j\cdot\boldsymbol{r}}$, $U_\omega(\boldsymbol{r}) = \alpha\sum_{j=1}^3 \omega^{j-1}e^{-i\boldsymbol{q}_j\cdot\boldsymbol{r}}$, and $\alpha = w_{\mathrm{AB}}/v_F k_\theta$. We focus on the first magic angle $\theta_{ABA} \approx 1.69^\circ$ where the renormalized velocity v^* vanishes [see the blue line in Fig. 2(b)]. Correspondingly, the two bands around charge neutrality become perfectly flat, as shown in Fig. 2(c). Interestingly, the single particle gap that separates the flat bands from remote ones is $E_{\mathrm{gap}} \approx 130$ meV, quite large when compared with the typical value of the Coulomb interaction screened by metallic gates [42]. The C_{3z} symmetry yields $\chi_{\Gamma 1}(0) = \chi_{\Gamma 3}(0) = 0$, while $\chi_{\Gamma 2}(0)$ is usually nonzero. The magic angle θ_{ABA} is exactly defined by $\chi_{\Gamma 2}(0) = 0$. As the spinor $\boldsymbol{\chi}_\Gamma(0)$ then fully vanishes at θ_{ABA}, the B-polarized flat band has an analytical expression

$$\boldsymbol{\chi}_{\boldsymbol{k}}(\boldsymbol{r}) = \bar{\eta}_{\boldsymbol{k}}(\bar{z})\boldsymbol{\chi}_\Gamma(\boldsymbol{r}), \tag{6}$$

where $\bar{z} = z^*$ and the antiholomorphic $\bar{\eta}_{\boldsymbol{k}}(\bar{z}) = \eta_{\boldsymbol{k}}^*(-z)$ is related to the meromorphic function

$$\eta_{\boldsymbol{k}}(z) = e^{ik_1 z/a_1}\frac{\vartheta_1[z/a_1 - k/b_2, \omega]}{\vartheta_1[z/a_1, \omega]}, \tag{7}$$

with the notation $k_1 = \boldsymbol{k}\cdot\boldsymbol{a}_1$ and $\vartheta_1[z, \omega]$ the Jacobi theta function [76], which vanishes at $z = 0$ and satisfies the Bloch periodicity. The self-periodic part of the wavefunction $\boldsymbol{u}_{\bar{k}}(\boldsymbol{r}) = e^{-i\boldsymbol{k}\cdot\boldsymbol{r}}\boldsymbol{\chi}_{\boldsymbol{k}}(\boldsymbol{r})$ is k antiholomorphic corresponding to an ideal flat band [39,48,91]. The Chern number of the band can be readily read off from the k-space boundary conditions

$$\boldsymbol{u}_{\bar{k}+\bar{b}_j}(\boldsymbol{r}) = e^{-i\boldsymbol{b}_j\cdot\boldsymbol{r}}e^{i\phi_{k,b_j}}\boldsymbol{u}_{\bar{k}}(\boldsymbol{r}), \tag{8}$$

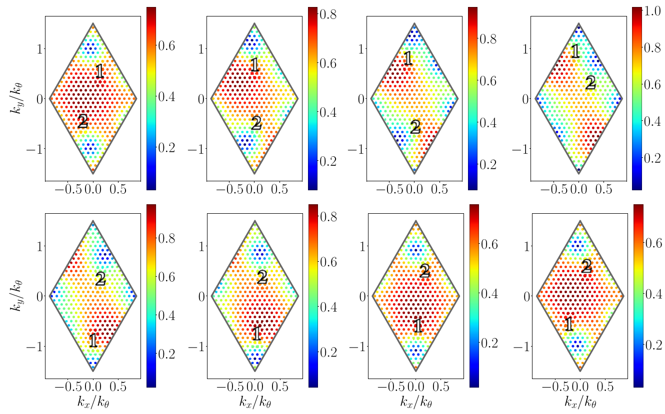

FIG. 3. Middle layer component $|\psi_{\boldsymbol{k}2}(\boldsymbol{r})|$ plotted in the BZ for different $\boldsymbol{r}$. From top left to bottom- right, the position $\boldsymbol{r}$ evolves between $\boldsymbol{r}_0 = (0.1, 0.3)$ (unit of $1/k_\theta$) and $\boldsymbol{r}_0 + \boldsymbol{a}_1$. $|\psi_{\boldsymbol{k}2}(\boldsymbol{r})|$ displays $C_A = 2$ indexed zeros in the BZ whose positions change with $\boldsymbol{r}$. Their pattern is invariant under a lattice translation but the two zeros are nonetheless swapped, akin to a Thouless pump but in reciprocal space.

where $\phi_{k,b_1} = -2\pi\bar{k}/\bar{b}_2 + \pi - \pi\bar{b}_1/\bar{b}_2$ and $\phi_{k,b_2} = \pi$ which implies $C_B = -1$ where the Chern number has been computed employing [48,55]

$$C = \frac{\phi_{\boldsymbol{k}_0+\boldsymbol{b}_2,\boldsymbol{b}_1} + \phi_{\boldsymbol{k}_0,\boldsymbol{b}_2} - \phi_{\boldsymbol{k}_0,\boldsymbol{b}_1} - \phi_{\boldsymbol{k}_0+\boldsymbol{b}_1,\boldsymbol{b}_2}}{2\pi}. \tag{9}$$

We turn to the exact solution for the A-polarized wavefunction $\boldsymbol{\psi}$. C_{3z} yields again $\psi_{\Gamma 1/3}(0) = 0$ at Γ and $\psi_{K/K'2}(0) = 0$ at K (K'), however $\psi_{\Gamma 2}(0)$ does not vanish at the magic angle. Nevertheless, we numerically find that $\psi_{K1}(0) = -\psi_{K3}(0)$, right at the magic angle θ_{ABA} which, combined with particle-hole symmetry P, proves that the two spinors are equal

$$\boldsymbol{\psi}_K(0) = \boldsymbol{\psi}_{K'}(0) \tag{10}$$

at θ_{ABA}. This remarkable identity allows us to exhibit an exact analytical expression for the A-polarized flat band (up to a $\boldsymbol{k}$-dependent prefactor) [76]

$$\boldsymbol{\psi}_{\boldsymbol{k}}(\boldsymbol{r}) = a_k\eta_{\boldsymbol{k}-\boldsymbol{q}_1}(z)\boldsymbol{\psi}_K(\boldsymbol{r}) + a_{-k}\eta_{\boldsymbol{k}+\boldsymbol{q}_1}(z)\boldsymbol{\psi}_{K'}(\boldsymbol{r}), \tag{11}$$

satisfying the Bloch periodicity, with the holomorphic function defined in Eq. (7) and $a_k = \vartheta_1[(k+q_1)/b_2, \omega]$. In Eq. (11), we set the K and K' points at $\pm\boldsymbol{q}_1$, respectively. Thanks to the following property of the theta function $\vartheta_1[-z, \omega] = -\vartheta_1[z, \omega]$, it is readily checked that the poles of $\eta_{\boldsymbol{k}\pm\boldsymbol{q}_1}(z)$ at $z = 0$ cancel each other in Eq. (11), as a result of Eq. (10), and the wavefunction is finite everywhere. We note that the corresponding unnormalized Bloch function $\boldsymbol{u}_k(\boldsymbol{r}) = e^{-i\boldsymbol{k}\cdot\boldsymbol{r}}\boldsymbol{\psi}_{\boldsymbol{k}}(\boldsymbol{r})$ is k holomorphic and thus constitutes an ideal flat band [39,48,91]. In addition, the momentum space boundary condition yields $\phi_{k,b_1} = 4\pi k/b_2 + 2\pi b_1/b_2$ and $\phi_{k,b_2} = 0$, resulting in a Chern number $C_A = 2$ and a total Chern number $C = C_A + C_B = +1$ associated with the triangular regions centered around the ABA site in Fig. 1(b). Remarkably, the Chern 2 band of Eq. (11) describes a color-entangled wavefunction [55,92] and, upon translation of a lattice vector $\boldsymbol{r}_0 \to \boldsymbol{r}_0 + \boldsymbol{a}_1$, the k-space zeros of $|\psi_{\boldsymbol{k}2}(\boldsymbol{r})|$ get swapped, see Fig. 3. The emergence of the Chern bands +2

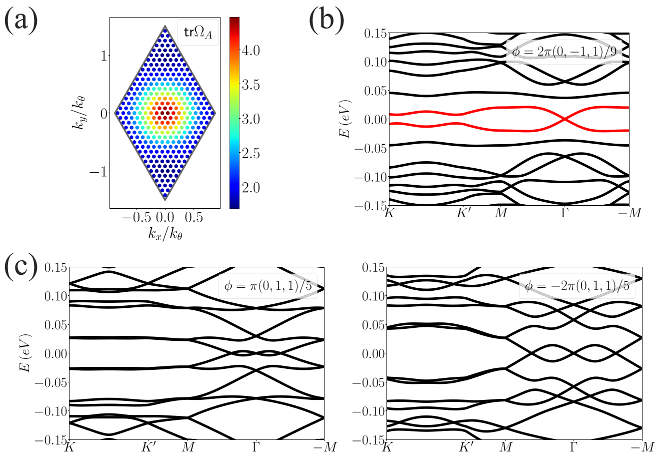

FIG. 4. (a) Trace of the non-Abelian Berry curvature for the A sublattice $\Lambda_z = +1$ (due to $C_{2z}T$ we have $\mathrm{tr}\Omega_B = -\mathrm{tr}\Omega_A$). Numerically, $\mathrm{Tr}\,\mathrm{tr}\, g = \mathrm{tr}\,\Omega$ is verified. (b) Spectrum obtained by moving away from AAA stacking along the $\mathbf{a}_2^{\mathrm{MM}} - \mathbf{a}_1^{\mathrm{MM}}$ direction. The bands highlighted in red carry a Chern value $+1$ in agreement with Fig. 1(b). (c) Fully connected spectra obtained along the domain wall $\mathbf{a}_1^{\mathrm{MM}} + \mathbf{a}_2^{\mathrm{MM}}$ direction. The spectra are computed at the magic angle $\theta_{AAA} \approx 0.75^\circ$, in the chiral limit $w_{\mathrm{AA}} = 0$.

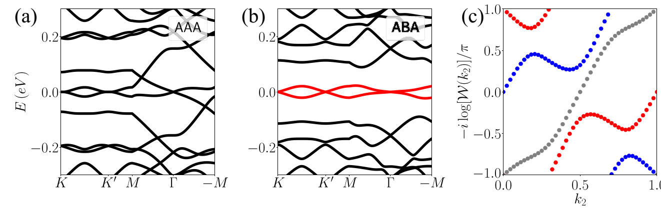

FIG. 5. Results for $w_{\mathrm{AA}}/w_{\mathrm{AB}} = 0.7$ and twist angle $\theta = 1.69^\circ$. (a) Fully connected spectrum at AAA. (b) Band structure at ABA. The two nearly flat bands (in red) split off clearly from the remote bands. (c) Wilson loop $\mathcal{W}(k_2)$ phase eigenvalues (red and blue dots) for the two nearly flat bands as a function of $k_2 = \boldsymbol{k}\cdot\boldsymbol{a}_2/2\pi$. Their sum (gray dots) winds by 2π corresponding to the total Chern number $+1$.

and -1 can be intuitively understood as a direct consequence of the original three Dirac cones of each layer, similar to twisted monobilayer graphene [71,93].

AAA stacking and domain wall lines. The local Hamiltonian $\mathcal{H}_{\mathrm{AAA}}$ describing the AAA points is obtained by setting $\boldsymbol{\phi} = 0$ in Eq. (1). It satisfies all symmetries [86]: $C_{2z}T$, C_{2x}, C_{3z} and particle-hole symmetry P, protecting the Dirac cones at K, K', and Γ. $C_{2z}T$ furthermore enforces [86] a fully connected spectrum as an odd number of Dirac cones cannot form isolated minibands [73,94–96]. In the chiral limit $w_{\mathrm{AA}} = 0$, $\mathcal{H}_{\mathrm{AAA}}$, in the basis $\Psi = (\psi_1 \quad \psi_2 \quad \psi_3 \quad \chi_1 \quad \chi_2 \quad \chi_3)^T$ takes the form

$$\frac{\mathcal{H}_{\mathrm{AAA}}(\boldsymbol{r})}{v_F k_\theta} = \begin{pmatrix} 0 & \mathcal{D}_2(\boldsymbol{r}) \\ \mathcal{D}_2^\dagger(\boldsymbol{r}) & 0 \end{pmatrix}, \tag{12}$$

where the operator reads

$$\mathcal{D}_2(\boldsymbol{r}) = \begin{pmatrix} -i\sqrt{2}\partial & U_{\omega^*}(\boldsymbol{r}) & 0 \\ U_{\omega^*}(-\boldsymbol{r}) & -i\sqrt{2}\partial & U_{\omega^*}(\boldsymbol{r}) \\ 0 & U_{\omega^*}(-\boldsymbol{r}) & -i\sqrt{2}\partial \end{pmatrix}, \tag{13}$$

and $U_{\omega^*}(\boldsymbol{r}) = U_\omega^*(-\boldsymbol{r})$. At the magic angle taking place at $\theta_{\mathrm{AAA}} \approx 0.75^\circ$, see the red line in Fig. 2(b), the spectrum shown in Fig. 2(d) is composed by a fourfold degenerate zero mode subspace and a renormalized Dirac cone located at Γ. Interestingly, the wavefunction of the zero modes can be exactly expressed in terms of meromorphic functions as shown in Ref. [85]. We focus here on the topological properties of the fourfold degenerate flat band sector. Away from the Γ point the flat bands are isolated and the degeneracy can be partially resolved by Λ_z which splits the fourfold degeneracy into two doublets with $\Lambda_z = \pm 1$. For a given sublattice the topological properties are characterized by the non-Abelian quantum geometric tensor $Q_{nm}^{ab}(\boldsymbol{k}) = \langle D_a u_{n\boldsymbol{k}} | D_b u_{m\boldsymbol{k}} \rangle$ with D_a the covariant derivative [97]. The non-Abelian trace condition [35] reads as $\mathrm{Tr}\,\mathrm{tr}\, g = \mathrm{tr}\,\Omega$ where Tr traces over space directions, whereas tr traces over the doublet subspace. Figure 4(a) shows the Berry curvature $\mathrm{tr}\,\Omega_A$; we check numerically that the trace condition is satisfied everywhere at the exclusion of the Γ point where the Berry curvature is ill defined. $C_{2z}T$ imposes that the two sublattice sectors yield opposite Berry curvature $\mathrm{tr}\Omega_A = -\mathrm{tr}\Omega_B$. The points AAA are however singular. The fourfold degeneracy is lifted by any small but finite $\boldsymbol{\phi}$ and the flat band sector with Chern number ± 1 is recovered, see Fig. 4(b). The Chern mosaic of Fig. 1(b) is thus largely governed by the topology of the ABA and BAB points.

Finally, the different topological regions extended around ABA and BAB meet along lines where the gap to the remote bands vanishes, Fig. 1(c). These lines form a triangular lattice originating from the AAA lattice sites as shown in Fig. 1(b). We prove [76] that, along these lines, the C_{2x} symmetry, combined with C_{3z}, yields a fully connected band structure for Eq. (1), as seen in Fig. 4(c). Breaking these symmetries can move the domain walls but not suppress them since the distinct topological domains must be separated by gap-closing contours.

Stability away from the chiral limit. Our predictions formally derived in the chiral limit are stable and persist for finite values of w_{AA}. Figure 5(b) shows that, at finite w_{AA}, the low-energy bands in ABA regions acquire a finite dispersion. However, the two flat bands highlighted in red in Fig. 5(b) are still characterized by a total Chern number $+1$ as shown by the winding 2π of the Wilson loop in Fig. 5(c). The Chern mosaic pattern depicted in Fig. 1(b) is in fact relatively insensitive to w_{AA} and remains intact upon increasing w_{AA} from zero to $w_{\mathrm{AA}} = w_{\mathrm{AB}}$.

Conclusions. In summary, we have demonstrated that in equal-twist angle trilayer graphene, the separation between length scales gives rise to a supermoiré lattice modulation. In this lattice, the local registry corresponds to twisting around AAA to ABA stacking, and exhibits local-to-local long-range variation. The local Hamiltonian which depends parametrically on the supermoiré lattice coordinate displays topologically distinct regions where the low-energy flat bands have quantized and opposite Chern numbers. We showed explicitly that the finite Chern number in ABA regions originates from a zero-mode doublet composed of a Chern $+2$ color-entangled wavefunction and a Chern -1 Landau level-like state. The regions of opposite Chern values are separated by topologically protected gap-closing lines, thus forming a mosaic Chern pattern. These lines of domain wall connect the AAA sites and exhibit a fully connected spectrum protected by C_{2x}. Some of our findings can be generalized to cases involving unequal twist angles, where a similar decoupling of length scales occurs. The large energy gap between flat and remote bands compared with the typical Coulomb energy scale makes ABA stacking eTTG an ideal playground for studying Fractional Chern insulators in higher Chern number bands.

Acknowledgments. We are grateful to Jie Wang, Andrei Bernevig, Jed Pixley, Nicolas Regnault, and Raquel Queiroz for insightful discussions. D.G. also acknowledges discussions held at the 2023 Quantum Geometry Working Group meeting that took place at the Flatiron institute where he was introduced to some of the concepts presented here. We acknowledge support by the French National Research Agency (project TWISTGRAPH, ANR-21-CE47-0018). The Flatiron Institute is a division of the Simons Foundation.

[1] E. Y. Andrei and A. H. MacDonald, Graphene bilayers with a twist, Nat. Mater. **19**, 1265 (2020).
[2] R. Bistritzer and A. H. MacDonald, Moiré bands in twisted double-layer graphene, Proc. Natl. Acad. Sci. USA **108**, 12233 (2011).
[3] R. Bistritzer and A. H. MacDonald, Moiré butterflies in twisted bilayer graphene, Phys. Rev. B **84**, 035440 (2011).
[4] J. M. B. Lopes dos Santos, N. M. R. Peres, and A. H. Castro Neto, Continuum model of the twisted graphene bilayer, Phys. Rev. B **86**, 155449 (2012).
[5] J. M. B. Lopes dos Santos, N. M. R. Peres, and A. H. Castro Neto, Graphene bilayer with a twist: Electronic structure, Phys. Rev. Lett. **99**, 256802 (2007).
[6] E. Suárez Morell, J. D. Correa, P. Vargas, M. Pacheco, and Z. Barticevic, Flat bands in slightly twisted bilayer graphene: Tight-binding calculations, Phys. Rev. B **82**, 121407(R) (2010).
[7] E. J. Mele, Commensuration and interlayer coherence in twisted bilayer graphene, Phys. Rev. B **81**, 161405(R) (2010).
[8] Y. Cao, V. Fatemi, S. Fang, K. Watanabe, T. Taniguchi, E. Kaxiras, and P. Jarillo-Herrero, Unconventional superconductivity in magic-angle graphene superlattices, Nature (London) **556**, 43 (2018).
[9] M. Yankowitz, S. Chen, H. Polshyn, Y. Zhang, K. Watanabe, T. Taniguchi, D. Graf, A. F. Young, and C. R. Dean, Tuning superconductivity in twisted bilayer graphene, Science **363**, 1059 (2019).
[10] X. Lu, P. Stepanov, W. Yang, M. Xie, M. A. Aamir, I. Das, C. Urgell, K. Watanabe, T. Taniguchi, G. Zhang, A. Bachtold, A. H. MacDonald, and D. K. Efetov, Superconductors, orbital magnets and correlated states in magic-angle bilayer graphene, Nature (London) **574**, 653 (2019).
[11] P. Stepanov, I. Das, X. Lu, A. Fahimniya, K. Watanabe, T. Taniguchi, F. H. Koppens, J. Lischner, L. Levitov, and D. K. Efetov, Untying the insulating and superconducting orders in magic-angle graphene, Nature (London) **583**, 375 (2020).
[12] Y. Saito, J. Ge, K. Watanabe, T. Taniguchi, and A. F. Young, Independent superconductors and correlated insulators in twisted bilayer graphene, Nat. Phys. **16**, 926 (2020).
[13] Y. Cao, V. Fatemi, A. Demir, S. Fang, S. L. Tomarken, J. Y. Luo, J. D. Sanchez-Yamagishi, K. Watanabe, T. Taniguchi, E. Kaxiras, R. C. Ashoori, and P. Jarillo-Herrero, Correlated insulator behaviour at half-filling in magic-angle graphene superlattices, Nature (London) **556**, 80 (2018).
[14] S. L. Tomarken, Y. Cao, A. Demir, K. Watanabe, T. Taniguchi, P. Jarillo-Herrero, and R. C. Ashoori, Electronic compressibility of magic-angle graphene superlattices, Phys. Rev. Lett. **123**, 046601 (2019).
[15] H. Polshyn, M. Yankowitz, S. Chen, Y. Zhang, K. Watanabe, T. Taniguchi, C. R. Dean, and A. F. Young, Large linear-in-temperature resistivity in twisted bilayer graphene, Nat. Phys. **15**, 1011 (2019).
[16] D. Wong, K. P. Nuckolls, M. Oh, B. Lian, Y. Xie, S. Jeon, K. Watanabe, T. Taniguchi, B. A. Bernevig, and A. Yazdani, Cascade of electronic transitions in magic-angle twisted bilayer graphene, Nature (London) **582**, 198 (2020).
[17] U. Zondiner, A. Rozen, D. Rodan-Legrain, Y. Cao, R. Queiroz, T. Taniguchi, K. Watanabe, Y. Oreg, F. von Oppen, A. Stern, E. Berg, P. Jarillo-Herrero, and S. Ilani, Cascade of phase transitions and Dirac revivals in magic-angle graphene, Nature (London) **582**, 203 (2020).
[18] Y. Cao, D. Chowdhury, D. Rodan-Legrain, O. Rubies-Bigorda, K. Watanabe, T. Taniguchi, T. Senthil, and P. Jarillo-Herrero, Strange metal in magic-angle graphene with near planckian dissipation, Phys. Rev. Lett. **124**, 076801 (2020).
[19] J. M. Park, Y. Cao, K. Watanabe, T. Taniguchi, and P. Jarillo-Herrero, Flavour Hund's coupling, Chern gaps and charge diffusivity in moiré graphene, Nature (London) **592**, 43 (2021).
[20] A. Jaoui, I. Das, G. Di Battista, J. Díez-Mérida, X. Lu, K. Watanabe, T. Taniguchi, H. Ishizuka, L. Levitov, and D. K. Efetov, Quantum critical behaviour in magic-angle twisted bilayer graphene, Nat. Phys. **18**, 633 (2022).
[21] N. Bultinck, E. Khalaf, S. Liu, S. Chatterjee, A. Vishwanath, and M. P. Zaletel, Ground state and hidden symmetry of magic-angle graphene at even integer filling, Phys. Rev. X **10**, 031034 (2020).
[22] B. Lian, Z.-D. Song, N. Regnault, D. K. Efetov, A. Yazdani, and B. A. Bernevig, Twisted bilayer graphene. IV. exact insulator ground states and phase diagram, Phys. Rev. B **103**, 205414 (2021).
[23] A. L. Sharpe, E. J. Fox, A. W. Barnard, J. Finney, K. Watanabe, T. Taniguchi, M. A. Kastner, and D. Goldhaber-Gordon, Emergent ferromagnetism near three-quarters filling in twisted bilayer graphene, Science **365**, 605 (2019).
[24] M. Serlin, C. L. Tschirhart, H. Polshyn, Y. Zhang, J. Zhu, K. Watanabe, T. Taniguchi, L. Balents, and A. F. Young, Intrinsic quantized anomalous Hall effect in a moiré heterostructure, Science **367**, 900 (2020).
[25] J. H. Pixley and E. Y. Andrei, Ferromagnetism in magic-angle graphene, Science **365**, 543 (2019).
[26] G. Chen, A. L. Sharpe, E. J. Fox, Y.-H. Zhang, S. Wang, L. Jiang, B. Lyu, H. Li, K. Watanabe, T. Taniguchi, Z. Shi, T. Senthil, D. Goldhaber-Gordon, Y. Zhang, and F. Wang, Tunable correlated Chern insulator and ferromagnetism in a Moirésuperlattice, Nature (London) **579**, 56 (2020).

[27] S.-Y. Li, Y. Zhang, Y.-N. Ren, J. Liu, X. Dai, and L. He, Experimental evidence for orbital magnetic moments generated by moiré-scale current loops in twisted bilayer graphene, Phys. Rev. B **102**, 121406(R) (2020).

[28] S. Grover, M. Bocarsly, A. Uri, P. Stepanov, G. D. Battista, I. Roy, J. Xiao, A. Y. Meltzer, Y. Myasoedov, K. Pareek, K. Watanabe, T. Taniguchi, B. Yan, A. Stern, E. Berg, D. K. Efetov, and E. Zeldov, Chern mosaic and berry-curvature magnetism in magic-angle graphene, Nat. Phys. **18**, 885 (2022).

[29] N. Bultinck, S. Chatterjee, and M. P. Zaletel, Mechanism for anomalous Hall ferromagnetism in twisted bilayer graphene, Phys. Rev. Lett. **124**, 166601 (2020).

[30] C. Repellin, Z. Dong, Y.-H. Zhang, and T. Senthil, Ferromagnetism in narrow bands of moiré superlattices, Phys. Rev. Lett. **124**, 187601 (2020).

[31] W.-Y. He, D. Goldhaber-Gordon, and K. T. Law, Giant orbital magnetoelectric effect and current-induced magnetization switching in twisted bilayer graphene, Nat. Commun. **11**, 1650 (2020).

[32] P. Potasz, M. Xie, and A. H. MacDonald, Exact diagonalization for magic-angle twisted bilayer graphene, Phys. Rev. Lett. **127**, 147203 (2021).

[33] Y. Xie, A. T. Pierce, J. M. Park, D. E. Parker, E. Khalaf, P. Ledwith, Y. Cao, S. H. Lee, S. Chen, P. R. Forrester, K. Watanabe, T. Taniguchi, A. Vishwanath, P. Jarillo-Herrero, and A. Yacoby, Fractional Chern insulators in magic-angle twisted bilayer graphene, Nature (London) **600**, 439 (2021).

[34] C. Repellin and T. Senthil, Chern bands of twisted bilayer graphene: Fractional Chern insulators and spin phase transition, Phys. Rev. Res. **2**, 023238 (2020).

[35] D. Parker, P. Ledwith, E. Khalaf, T. Soejima, J. Hauschild, Y. Xie, A. Pierce, M. P. Zaletel, A. Yacoby, and A. Vishwanath, Field-tuned and zero-field fractional Chern insulators in magic angle graphene, arXiv:2112.13837.

[36] G. Tarnopolsky, A. J. Kruchkov, and A. Vishwanath, Origin of magic angles in twisted bilayer graphene, Phys. Rev. Lett. **122**, 106405 (2019).

[37] J. Liu, J. Liu, and X. Dai, Pseudo Landau level representation of twisted bilayer graphene: Band topology and implications on the correlated insulating phase, Phys. Rev. B **99**, 155415 (2019).

[38] F. K. Popov and A. Milekhin, Hidden wave function of twisted bilayer graphene: The flat band as a Landau level, Phys. Rev. B **103**, 155150 (2021).

[39] P. J. Ledwith, G. Tarnopolsky, E. Khalaf, and A. Vishwanath, Fractional Chern insulator states in twisted bilayer graphene: An analytical approach, Phys. Rev. Res. **2**, 023237 (2020).

[40] O. Vafek and J. Kang, Renormalization group study of hidden symmetry in twisted bilayer graphene with coulomb interactions, Phys. Rev. Lett. **125**, 257602 (2020).

[41] B. A. Bernevig, Z.-D. Song, N. Regnault, and B. Lian, Twisted bilayer graphene. I. matrix elements, approximations, perturbation theory, and a $k \cdot p$ two-band model, Phys. Rev. B **103**, 205411 (2021).

[42] B. A. Bernevig, Z.-D. Song, N. Regnault, and B. Lian, Twisted bilayer graphene. III. Interacting Hamiltonian and exact symmetries, Phys. Rev. B **103**, 205413 (2021).

[43] E. Khalaf, A. J. Kruchkov, G. Tarnopolsky, and A. Vishwanath, Magic angle hierarchy in twisted graphene multilayers, Phys. Rev. B **100**, 085109 (2019).

[44] A. Abouelkomsan, Z. Liu, and E. J. Bergholtz, Particle-hole duality, emergent fermi liquids, and fractional Chern insulators in moiré flatbands, Phys. Rev. Lett. **124**, 106803 (2020).

[45] Y. Ren, Q. Gao, A. H. MacDonald, and Q. Niu, WKB estimate of bilayer graphene's magic twist angles, Phys. Rev. Lett. **126**, 016404 (2021).

[46] E. Khalaf, S. Chatterjee, N. Bultinck, M. P. Zaletel, and A. Vishwanath, Charged skyrmions and topological origin of superconductivity in magic-angle graphene, Sci. Adv. **7**, eabf5299 (2021).

[47] P. J. Ledwith, E. Khalaf, and A. Vishwanath, Strong coupling theory of magic-angle graphene: A pedagogical introduction, Ann. Phys. **435**, 168646 (2021).

[48] J. Wang, Y. Zheng, A. J. Millis, and J. Cano, Chiral approximation to twisted bilayer graphene: Exact intravalley inversion symmetry, nodal structure, and implications for higher magic angles, Phys. Rev. Res. **3**, 023155 (2021).

[49] Y. Sheffer and A. Stern, Chiral magic-angle twisted bilayer graphene in a magnetic field: Landau level correspondence, exact wave functions, and fractional Chern insulators, Phys. Rev. B **104**, L121405 (2021).

[50] Z.-D. Song and B. A. Bernevig, Magic-angle twisted bilayer graphene as a topological heavy fermion problem, Phys. Rev. Lett. **129**, 047601 (2022).

[51] Y. Sheffer, R. Queiroz, and A. Stern, Symmetries as the guiding principle for flattening bands of Dirac fermions, Phys. Rev. X **13**, 021012 (2023).

[52] M. Barkeshli and X.-L. Qi, Topological nematic states and non-abelian lattice dislocations, Phys. Rev. X **2**, 031013 (2012).

[53] Y.-L. Wu, N. Regnault, and B. A. Bernevig, Bloch model wave functions and pseudopotentials for all fractional Chern insulators, Phys. Rev. Lett. **110**, 106802 (2013).

[54] Y.-L. Wu, N. Regnault, and B. A. Bernevig, Haldane statistics for fractional Chern insulators with an arbitrary Chern number, Phys. Rev. B **89**, 155113 (2014).

[55] J. Wang, S. Klevtsov, and Z. Liu, Origin of model fractional Chern insulators in all topological ideal flatbands: Explicit color-entangled wavefunction and exact density algebra, Phys. Rev. Res. **5**, 023167 (2023).

[56] X. Zhang, K.-T. Tsai, Z. Zhu, W. Ren, Y. Luo, S. Carr, M. Luskin, E. Kaxiras, and K. Wang, Correlated insulating states and transport signature of superconductivity in twisted trilayer graphene superlattices, Phys. Rev. Lett. **127**, 166802 (2021).

[57] A. Uri, S. C. de la Barrera, M. T. Randeria, D. Rodan-Legrain, T. Devakul, P. J. D. Crowley, N. Paul, K. Watanabe, T. Taniguchi, R. Lifshitz, L. Fu, R. C. Ashoori, and P. Jarillo-Herrero, Superconductivity and strong interactions in a tunable moiré quasiperiodic crystal, arXiv:2302.00686.

[58] J. M. Park, Y. Cao, K. Watanabe, T. Taniguchi, and P. Jarillo-Herrero, Tunable strongly coupled superconductivity in magic-angle twisted trilayer graphene, Nature (London) **590**, 249 (2021).

[59] Y. Cao, J. M. Park, K. Watanabe, T. Taniguchi, and P. Jarillo-Herrero, Pauli-limit violation and re-entrant superconductivity in moiré graphene, Nature (London) **595**, 526 (2021).

[60] Z. Hao, A. M. Zimmerman, P. Ledwith, E. Khalaf, D. H. Najafabadi, K. Watanabe, T. Taniguchi, A. Vishwanath, and P. Kim, Electric field–tunable superconductivity in alternating-twist magic-angle trilayer graphene, Science **371**, 1133 (2021).

[61] H. Kim, Y. Choi, C. Lewandowski, A. Thomson, Y. Zhang, R. Polski, K. Watanabe, T. Taniguchi, J. Alicea, and S. Nadj-Perge, Evidence for unconventional superconductivity in twisted trilayer graphene, Nature (London) **606**, 494 (2022).

[62] X. Liu, N. J. Zhang, K. Watanabe, T. Taniguchi, and J. I. A. Li, Isospin order in superconducting magic-angle twisted trilayer graphene, Nat. Phys. **18**, 522 (2022).

[63] S. Carr, C. Li, Z. Zhu, E. Kaxiras, S. Sachdev, and A. Kruchkov, Ultraheavy and ultrarelativistic Dirac quasiparticles in sandwiched graphenes, Nano Lett. **20**, 3030 (2020).

[64] D. Călugăru, F. Xie, Z.-D. Song, B. Lian, N. Regnault, and B. A. Bernevig, Twisted symmetric trilayer graphene: Single-particle and many-body hamiltonians and hidden nonlocal symmetries of trilayer moiré systems with and without displacement field, Phys. Rev. B **103**, 195411 (2021).

[65] F. Xie, N. Regnault, D. Călugăru, B. A. Bernevig, and B. Lian, Twisted symmetric trilayer graphene. II. Projected hartree-fock study, Phys. Rev. B **104**, 115167 (2021).

[66] D. Guerci, P. Simon, and C. Mora, Higher-order Van Hove singularity in magic-angle twisted trilayer graphene, Phys. Rev. Res. **4**, L012013 (2022).

[67] M. Christos, S. Sachdev, and M. S. Scheurer, Correlated insulators, semimetals, and superconductivity in twisted trilayer graphene, Phys. Rev. X **12**, 021018 (2022).

[68] S. Chen, M. He, Y.-H. Zhang, V. Hsieh, Z. Fei, K. Watanabe, T. Taniguchi, D. H. Cobden, X. Xu, C. R. Dean, and M. Yankowitz, Electrically tunable correlated and topological states in twisted monolayer–bilayer graphene, Nat. Phys. **17**, 374 (2021).

[69] M. He, Y.-H. Zhang, Y. Li, Z. Fei, K. Watanabe, T. Taniguchi, X. Xu, and M. Yankowitz, Competing correlated states and abundant orbital magnetism in twisted monolayer-bilayer graphene, Nat. Commun. **12**, 4727 (2021).

[70] H. Polshyn, Y. Zhang, M. A. Kumar, T. Soejima, P. Ledwith, K. Watanabe, T. Taniguchi, A. Vishwanath, M. P. Zaletel, and A. F. Young, Topological charge density waves at half-integer filling of a moiré superlattice, Nat. Phys. **18**, 42 (2022).

[71] P. J. Ledwith, A. Vishwanath, and E. Khalaf, Family of ideal Chern flatbands with arbitrary Chern number in chiral twisted graphene multilayers, Phys. Rev. Lett. **128**, 176404 (2022).

[72] Z. Zhu, S. Carr, D. Massatt, M. Luskin, and E. Kaxiras, Twisted trilayer graphene: A precisely tunable platform for correlated electrons, Phys. Rev. Lett. **125**, 116404 (2020).

[73] Y. Mao, D. Guerci, and C. Mora, Supermoiré low-energy effective theory of twisted trilayer graphene, Phys. Rev. B **107**, 125423 (2023).

[74] T. Cea, P. A. Pantaleón, and F. Guinea, Band structure of twisted bilayer graphene on hexagonal boron nitride, Phys. Rev. B **102**, 155136 (2020).

[75] J. Shi, J. Zhu, and A. H. MacDonald, Moiré commensurability and the quantum anomalous Hall effect in twisted bilayer graphene on hexagonal boron nitride, Phys. Rev. B **103**, 075122 (2021).

[76] See Supplemental Material at http://link.aps.org/supplemental/10.1103/PhysRevResearch.6.L022025 for provides an in-depth examination of the adiabatic Hamiltonian, covering its symmetries and notation. Additionally, it discusses fundamental properties of the Jacobi theta function and computes the derivative of the Wronskian.

[77] J. M. Luttinger and W. Kohn, Motion of electrons and holes in perturbed periodic fields, Phys. Rev. **97**, 869 (1955).

[78] G. Bastard, Superlattice band structure in the envelope-function approximation, Phys. Rev. B **24**, 5693 (1981).

[79] S. R. White and L. J. Sham, Electronic properties of flat-band semiconductor heterostructures, Phys. Rev. Lett. **47**, 879 (1981).

[80] G. Bastard, Theoretical investigations of superlattice band structure in the envelope-function approximation, Phys. Rev. B **25**, 7584 (1982).

[81] D. L. Smith and C. Mailhiot, Theory of semiconductor superlattice electronic structure, Rev. Mod. Phys. **62**, 173 (1990).

[82] T. Devakul, P. J. Ledwith, L.-Q. Xia, A. Uri, S. C. de la Barrera, P. Jarillo-Herrero, and L. Fu, Magic-angle helical trilayer graphene, Sci. Adv. **9**, eadi6063 (2023).

[83] N. Nakatsuji, T. Kawakami, and M. Koshino, Multiscale lattice relaxation in general twisted trilayer graphenes, Phys. Rev. X **13**, 041007 (2023).

[84] F. K. Popov and G. Tarnopolsky, Magic angle butterfly in twisted trilayer graphene, Phys. Rev. Res. **5**, 043079 (2023).

[85] F. K. Popov and G. Tarnopolsky, Magic angles in equal-twist trilayer graphene, arXiv:2303.15505.

[86] C. Mora, N. Regnault, and B. A. Bernevig, Flatbands and perfect metal in trilayer moiré graphene, Phys. Rev. Lett. **123**, 026402 (2019).

[87] P. J. Ledwith, A. Vishwanath, and D. E. Parker, Vortexability: A unifying criterion for ideal fractional Chern insulators, Phys. Rev. B **108**, 205144 (2023).

[88] B. Mera and T. Ozawa, Uniqueness of Landau levels and their analogs with higher Chern numbers, arXiv:2304.00866.

[89] J. Wang, J. Cano, A. J. Millis, Z. Liu, and B. Yang, Exact Landau level description of geometry and interaction in a flatband, Phys. Rev. Lett. **127**, 246403 (2021).

[90] A. Parhizkar and V. Galitski, A generic topological criterion for flat bands in two dimensions, arXiv:2301.00824.

[91] B. Estienne, N. Regnault, and V. Crépel, Ideal Chern bands are Landau levels in curved space, Phys. Rev. Res. **5**, L032048 (2023).

[92] J. Dong, P. J. Ledwith, E. Khalaf, J. Y. Lee, and A. Vishwanath, Many-body ground states from decomposition of ideal higher Chern bands: Applications to chirally twisted graphene multilayers, Phys. Rev. Res. **5**, 023166 (2023).

[93] J. Wang and Z. Liu, Hierarchy of ideal flatbands in chiral twisted multilayer graphene models, Phys. Rev. Lett. **128**, 176403 (2022).

[94] Z. Song, Z. Wang, W. Shi, G. Li, C. Fang, and B. A. Bernevig, All magic angles in twisted bilayer graphene are topological, Phys. Rev. Lett. **123**, 036401 (2019).

[95] J. Ahn, S. Park, and B.-J. Yang, Failure of nielsen-ninomiya theorem and fragile topology in two-dimensional systems with space-time inversion symmetry: Application to twisted bilayer graphene at magic angle, Phys. Rev. X **9**, 021013 (2019).

[96] J. Cano, S. Fang, J. H. Pixley, and J. H. Wilson, Moiré superlattice on the surface of a topological insulator, Phys. Rev. B **103**, 155157 (2021).

[97] R. Resta, Geometry and topology in many-body physics (2020), arXiv:2006.15567.